IEEE Access
Multidisciplinary | Rapid Review | Open Access Journal

Received August 28, 2019, accepted September 7, 2019, date of publication September 16, 2019,
date of current version September 30, 2019.

Digital Object Identifier 10.1109/ACCESS.2019.2941712

Design and Control of a Dual-Stage Actuation Active Vibration Isolation System

BO ZHAO, WEIJIA SHI, AND JIUBIN TAN

Center of Ultra-Precision Optoelectronic Instrument Engineering, Harbin Institute of Technology, Harbin 150080, China
Key Lab of Ultra-Precision Intelligent Instrumentation, Ministry of Industry and Information Technology, Harbin Institute of Technology, Harbin 150080, China

Corresponding author: Weijia Shi (shiweijia@hit.edu.cn)

This work was supported in part by the National Major Scientific Instruments and Equipment Development Special Funds of China under Grant 2018YFF01012003, and in part by the National Natural Science Foundation of China under Grant 51975160.

ABSTRACT Active vibration isolation system is used in various fields to reduce the vibrations transmitted. In this paper, a novel dual-stage actuator is proposed, which combines a voice coil motor and a piezoelectric actuator. The proposed dual-stage actuator maintains the advantages, in terms of the long stroke, the high precision, and the wide band. The dual-stage actuation active vibration isolation system (DSA-AVIS) with the proposed dual-stage actuator is initially modeled. The characteristic of the DSA-AVIS is subsequently analyzed. H_∞ controller is finally designed to consider the vibration isolation performance and the output range of the actuators. The experimental results indicate that the closed-loop transmissibility of the DSA-AVIS is less than -18 dB from 0 to 100 Hertz.

INDEX TERMS Active vibration isolation system, dual-stage actuation, H-infinite, piezoelectric actuator, voice coil motor.

I. INTRODUCTION

Vibration isolation has been of great interest in the academic and industrial areas of lithography machines [1], high-precision measuring instruments [2], [3], automobiles [4], [5], aerospace [6], [7], civil structures [8], and floating raft [9], [10]. Passive vibration isolation systems, such as springs, are often sufficient for high-frequency isolation in many applications [11]. However, they do not perform well in the low-frequency range. To improve the vibration isolation performance, especially in the low-frequency range, the active vibration isolation system (AVIS) is therefore proposed. An AVIS is composed of sensors, actuators, control system, and passive vibration isolation components. The AVIS is of higher cost but it can perform better than passive vibration isolation system.

The actuators play an important role in the AVIS. A variety of actuators have been studied and used in AVIS, such as, hydraulic actuators, voice coil motor (VCM), and piezoelectric (PZT) actuators. The VCM, an electromagnetic actuator driven by the Lorentz force, has been widely applied in AVIS, with zero stiffness, long motion stroke, simple structure, small size [12]. D.-P. Hong et al. proposed a VCM for active vibration isolator, whose natural frequency is 47 Hz [13]. M. Kim et al. proposed a novel VCM actuator, which uses a Halbach magnet array to produce a high force constant, for an AVIS [14]. The manufactured AVIS was able to properly attenuate vibration with feedback control. S. Ito and G. Schitter proposed an atomic force microscope capable of vibration isolation with its internal Z-axis VCMs moving the AFM probe [15]. However, the VCM suffers from some disadvantages. The VCM works well in the frequency of zero to tens of Hertz, but its high frequency dynamics is not good enough [16]. Moreover, for the micro vibration isolation, the resolution of the VCM is not high enough as well [17], [18].

In recent years, the PZT begins to be attractive in the field of vibration isolation because of the advantages in terms of wide band, high precision, fast response, and light weight. Y. Zhang et al. proposed a vibration isolator which is composed of the active PZT and the passive rubber isolator and the active PZT can eliminate the resonance peak significantly [19]. C. Wang et al. proposed a Stewart platform with PZTs for micro-vibration isolation. The Stewart platform can achieve 30 dB attenuation of periodical disturbances and 10-20 dB attenuation of random disturbances in the frequency range of 5-200 Hz [20]. J. Fu et al. designed a hybrid isolator using PZT and magnetorheological elastomer isolator to suppress the wide-frequency vibration in precision platform. The results showed that the hybrid isolator can attenuate full

The associate editor coordinating the review of this manuscript and approving it for publication was Yingxiang Liu.

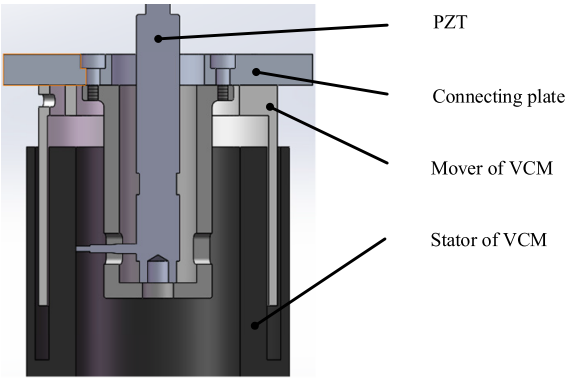

FIGURE 1. Schematic of the dual-stage actuator.

frequency vibration effectively [21]. The most badly influenced disadvantage of the PZT is the short stroke [22].

The paper aims at proposing a novel dual-stage active vibration isolator, which simultaneously utilizes a voice coil motor and a piezoelectric stack in series. The dual-stage actuation concept has been proposed in the precision positioning systems, such as in [17], [22], [23], and [24]. But in the field of vibration isolation, dual-stage actuation has not been fully studied. The utilization of the piezoelectric stack can introduce a novel anti-resonance, at which frequency the dual actuator naturally maintains an effect of absorbing vibration. The proposed dual-stage actuator is applied to an AVIS to achieve the wide band and the high-performance vibration isolation. The dual-stage actuation active vibration isolation system (DSA-AVIS) is initially proposed and mathematically modeled. The $H\infty$ controller is then designed based on characteristics of the DSA-AVIS. The vibration isolation performance of the DSA-AVIS is finally verified. The dual-stage actuator has the advantages, in terms of long stroke, high precision and wide band. The proposed DSA-AVIS has good vibration isolation performance in both low frequency and high frequency.

This paper is organized as follows. In Section II, the DSA-AVIS is described and modeled. Section III presents controller design. Experiment is provided in Section IV. Finally, the conclusions are drawn in Section V.

II. SYSTEM DESCRIPTION AND DYNAMIC MODELING

A. CONFIGURATION OF THE DSA-AVIS

The proposed dual-stage actuator is created by connecting a VCM serially onto a PZT, as shown in **Figure 1**. The PZT actuator here is used in a form of a PZT stack. The VCM has long motion stroke with zero stiffness. However, it only works in low frequency band and its resolution is not high enough for micro vibration isolation. The PZT has the advantages of wide band and extremely high resolution, but the stroke of the PZT is only a few tens of microns. The dual-stage actuator combines the advantages of them and obtains wide control frequency band, high resolution and long motion stroke in the active vibration isolation system.

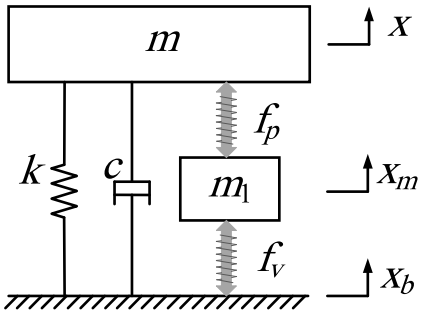

FIGURE 2. Schematic of the DSA-AVIS.

The schematic of a DSA-AVIS is shown in **Figure 2**, where m is the mass of the payload, m_1 is the mass of the VCM mover, the PZT and connecting device, k and c are the stiffness and the damping coefficient of the passive vibration isolation system, respectively, f_v and f_p are the VCM force and the PZT force, respectively, and $x, x_\mathrm{b}, x_\mathrm{m}$ are the displacement of the payload, the base and the mover.

B. DYNAMIC MODELING OF THE DSA-AVIS

The equations of the motion of the DSA-AVIS are given by

$$\begin{cases} m_1\ddot{x}_m = f_v - f_p \\ m\ddot{x} = f_p - k\,(x - x_b) - c\,(\dot{x} - \dot{x}_b)\,. \end{cases} \tag{1}$$

The constitutive equation of the VCM follows from Faraday's law

$$f_v = NB\pi\, dI = k_i I\,, \tag{2}$$

where N is the number of coils turns, B is the average magnetic induction of the air gap, d is the diameter of coil, I is the current value of the coil and $k_i = NB\pi d$ is the thrust coefficient of the VCM.

Based on one-dimensional piezoelectric equation, the longitudinal stress of the piezoelectric ceramic piece is

$$\sigma = E_p\,(\varepsilon - d_{33}E)\,, \tag{3}$$

where E_p is elasticity modulus, ε is longitudinal strain, d_{33} is longitudinal piezoelectric deformation coefficient, and E is longitudinal electric field intensity. The operating voltage and the longitudinal displacement of the PZT are given by

$$U = Eh, \tag{4}$$

$$\delta = n\varepsilon h, \tag{5}$$

where h is the thickness of individual layers of a stack actuator, and n is the number of stacked ceramic layers. The output force of the PZT can be derived by

$$\begin{aligned} f_p &= -A\sigma = AE_p\left(\frac{d_{33}U}{h} - \frac{\delta}{nh}\right) = \frac{AE_p d_{33}}{h}U - \frac{AE_p}{nh}\delta \\ &= k_u U - k_p\delta, \end{aligned} \tag{6}$$

where A is the area of the piezoelectric ceramic piece, $k_u = AE_p d_{33}/h$ and $k_p = AE_p/(nh)$ are constant.

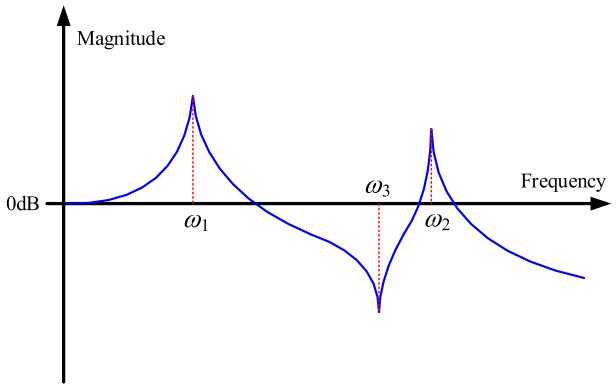

FIGURE 3. Conceptual Bode diagram of the passive transmissibility.

By substituting (2) and (6) into (1), and noting $\delta = x - x_m$, the dynamic equations become

$$\begin{cases} m_1\ddot{x}_m = k_i I - k_u U + k_p (x - x_m) \\ m\ddot{x} = k_u U - k_p (x - x_m) - k (x - x_b) - c (\dot{x} - \dot{x}_b) ., \end{cases} \tag{7}$$

C. CHARACTERISTIC ANALYSIS

Let control inputs become zero, namely, $I = 0$ and $U = 0$, and the Laplace transform of (7) can be written as

$$\begin{cases} m_1 s^2 X_m(s) = k_p X(s) - k_p X_m(s) \\ m s^2 X(s) = -k_p X(s) + k_p X_m(s) - kX(s) + kX_b(s) \\ \qquad -csX(s) + csX_b(s). \end{cases} \tag{8}$$

The transmissibility which is defined by the transfer function from the base displacement x_b to the payload displacement x, is used to evaluate the vibration isolation performance. The passive transmissibility can be driven from (8) as

$$\frac{X(s)}{X_b(s)} = \frac{m_1 c s^3 + m_1 k s^2 + k_p c s + k k_p}{m m_1 s^4 + m_1 c s^3 + \left(m k_p + m_1 k + m_1 k_p\right) s^2 + k_p c s + k k_p}. \tag{9}$$

To analyze frequency characteristic, the damping coefficient can be neglected since it is small. The passive transmissibility can be rewritten as

$$\begin{aligned} \frac{X(s)}{X_b(s)} &= \frac{m_1 k s^2 + k k_p}{m m_1 s^4 + \left(m k_p + m_1 k + m_1 k_p\right) s^2 + k k_p} \\ &= \frac{k}{m} \frac{s^2 + \omega_3^2}{\left(s^2 + \omega_1^2\right)\left(s^2 + \omega_2^2\right)} \end{aligned} \tag{10}$$

where $\omega_1\omega_2 = \omega_3\sqrt{k/m}$, $\omega_1^2 + \omega_2^2 = \omega_3^2 + k/m + k_p/m$, and $\omega_3 = \sqrt{k_p/m}$.

Figure 3 shows conceptual Bode diagram of the passive transmissibility. There are two resonant frequencies, ω_1 and ω_2. When the frequency of the base vibration is around ω_1 or ω_2, the vibration is greatly amplified. Therefore, the active control is required around the resonant frequencies. When the frequency of the base vibration equals to ω_3, the ratio of the payload displacement x and the base displacement x_b subsequently becomes zero; the vibration is therefore isolated entirely. This phenomenon is known as anti-resonance and ω_3 is therefore named as anti- resonance frequency [25]. The mover of the VCM, the PZT and the connecting device can be considered as a dynamic vibration absorber (DVA). For the vibration whose frequency is around anti-resonance frequency ω_3, active control is not required. The anti-resonance frequency ω_3 can be adjusted by adjusting the mass of the mover of the VCM or the mass of the connecting device and this DVA can be utilized to save energy. Furthermore, due to $\omega_1\omega_2 = \omega_3\sqrt{k/m}$, resonant frequencies ω_1 and ω_2 can be adjusted by adjusting the stiffness of the passive vibration isolation system.

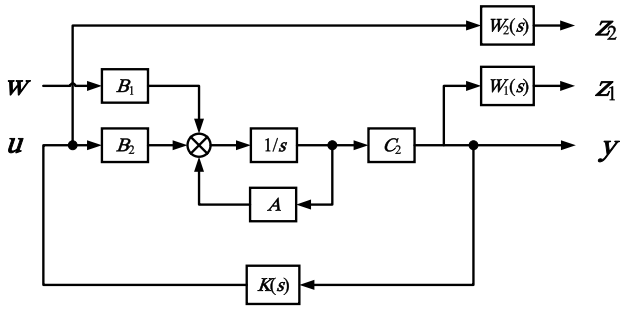

FIGURE 4. Control block diagram.

III. CONTROL SYNTHESIS

The active control is designed to suppress the extra vibration, whose frequency is around ω_1 or ω_2. According to the characteristics of the DSA-AVIS as shown in **Figure 3**, H_∞ control is selected, because the transfer function can be shaped with proper weighting functions. The displacement of the payload x is selected as feedback signal. Based on (7), the DSA-AVIS model in state space can be obtained

$$\begin{aligned} \dot{\boldsymbol{x}} &= \boldsymbol{A}\boldsymbol{x} + \boldsymbol{B_1}\boldsymbol{w} + \boldsymbol{B_2}\boldsymbol{u} \\ \boldsymbol{y} &= \boldsymbol{C_2}\boldsymbol{x} \end{aligned} \tag{11}$$

where $\boldsymbol{x} = [x_m, \dot{x}_m, x, \dot{x}]$ is state variable, $\boldsymbol{w} = [x_b, \dot{x}_b]^{\mathrm{T}}$ is disturbance input, $\boldsymbol{u} = [I, U]^{\mathrm{T}}$ is control input, and $\boldsymbol{y} = x$ is measured output, the other matrixes are described as

$$\boldsymbol{A} = \begin{bmatrix} \boldsymbol{A}_{11} & \boldsymbol{A}_{12} \\ \boldsymbol{A}_{21} & \boldsymbol{A}_{22} \end{bmatrix}, \boldsymbol{B}_1 = \begin{bmatrix} \boldsymbol{B}_{11} \\ \boldsymbol{B}_{12} \end{bmatrix}, \boldsymbol{B}_2 = \begin{bmatrix} \boldsymbol{B}_{21} \\ \boldsymbol{B}_{22} \end{bmatrix},$$

$$\boldsymbol{C} = \begin{bmatrix} \boldsymbol{C}_1 \\ \boldsymbol{C}_2 \end{bmatrix}, \boldsymbol{A}_{11} = \begin{bmatrix} 0 & 1 \\ -\dfrac{k_p}{m_1} & 0 \end{bmatrix}, \boldsymbol{A}_{12} = \begin{bmatrix} 0 & 0 \\ \dfrac{k_p}{m_1} & 0 \end{bmatrix},$$

$$\boldsymbol{A}_{21} = \begin{bmatrix} 0 & 0 \\ \dfrac{k_p}{m} & 0 \end{bmatrix}, \boldsymbol{A}_{22} = \begin{bmatrix} 0 & 1 \\ -\dfrac{k + k_p}{m} & -\dfrac{c}{m} \end{bmatrix},$$

$$\boldsymbol{B}_{11} = \boldsymbol{0}_{2\times 2}, \boldsymbol{B}_{12} = \begin{bmatrix} 0 & 0 \\ \dfrac{k}{m} & \dfrac{c}{m} \end{bmatrix}, \boldsymbol{B}_{21} = \begin{bmatrix} 0 & 0 \\ \dfrac{k_i}{m_1} & -\dfrac{k_u}{m_1} \end{bmatrix},$$

$$\boldsymbol{B}_{22} = \begin{bmatrix} 0 & 0 \\ 0 & \dfrac{k_u}{m} \end{bmatrix}, \boldsymbol{C}_1 = \boldsymbol{0}_{2\times 1}, \boldsymbol{C}_2 = \begin{bmatrix} 0 \\ 1 \end{bmatrix}.$$

The control block diagram is shown in **Figure 4**, where z_1 and z_2 are control outputs. Weighting functions $\boldsymbol{W}_1$ and $\boldsymbol{W}_2$ reflect the disturbance suppression performance and the output range of the actuators, respectively. Let $\boldsymbol{T}_{\mathrm{yw}}$ and $\boldsymbol{T}_{\mathrm{uw}}$ denote the transfer function from disturbance input $\boldsymbol{w}$ to measured output $\boldsymbol{y}$ and the transfer function from disturbance input $\boldsymbol{w}$ to control input $\boldsymbol{u}$. The controller $\boldsymbol{K}$ is obtained by minimizing the $H\infty$ norm of the transfer function from $\boldsymbol{w}$ to $\boldsymbol{z_1}$ and $\boldsymbol{z_2}$, that is

$$\left\| \begin{matrix} \boldsymbol{W_1 T_{yw}} \\ \boldsymbol{W_2 T_{uw}} \end{matrix} \right\|_{\infty}. \tag{12}$$

The term $\boldsymbol{W_1}$ is the relative weighting function of the payload displacement. In order to suppress the disturbance, we choose a relative higher gain in $\boldsymbol{W_1}$ in the frequency around the resonant frequencies of the DSA-AVIS to guarantee isolation performance; a relative lower gain in $\boldsymbol{W_1}$ is considered in the frequency around ω_3 and in the high frequency. The expression of $\boldsymbol{W_1}$ is

$$\boldsymbol{W_1} = \frac{k_1\left(s^2 + 2\xi_1\omega_3 s + \omega_3^2\right)}{(s+\omega_4)\left(s^2 + 2\xi_2\omega_2 s + \omega_2^2\right)}. \tag{13}$$

where ω_2 and ω_3 are aforementioned in section 2.3, and k_1, ξ_1, ξ_2, and ω_4 are adjustment parameters. The conceptual Bode diagram of $\boldsymbol{W_1}$ is shown in **Figure 5(a)**.

The term $\boldsymbol{W_2}$ is the weighting function of the control input. The gain in $\boldsymbol{W_2}$ should be low enough in the concerned isolation frequency range to make sure a sufficient feedback control force can be provided by the actuator. However, a smaller gain in $\boldsymbol{W_2}$ is not always better because the control force should not exceed the peak output force of the actuator in practical application. A relative higher gain in $\boldsymbol{W_2}$ was considered in order to reduce the control force in the inconsequential frequency range. The expression of $\boldsymbol{W_2}$ is given as

$$\begin{aligned} \boldsymbol{W_2} &= \begin{bmatrix} W_{21} & 0 \\ 0 & W_{22} \end{bmatrix} \\ W_{21} &= \frac{k_2\left(s^2 + 2\xi_3\omega_5 s + \omega_5^2\right)}{s^2 + 2\xi_4\omega_6 s + \omega_6^2} \\ W_{22} &= \frac{k_3\,(s+\omega_7)\left(s^2 + 2\xi_5\omega_2 s + \omega_2^2\right)}{(s+\omega_8)\left(s^2 + 2\xi_6\omega_3 s + \omega_3^2\right)}. \end{aligned} \tag{14}$$

where ω_2 and ω_3 are aforementioned in section 2.3, and k_2, $k_3, \xi_3, \xi_4, \xi_5, \xi_6, \omega_5, \omega_6, \omega_7$ and ω_8 are adjustment parameters. The conceptual Bode diagram of $\boldsymbol{W_2}$ is shown in **Figure 5(b)**.

The design of the weight functions of an H-inf controller can guarantee that the DSA-AVIS maintain different gains within different bandwidth, which can effectively eliminate the resonance peaks with lowest conservative performance. The PID controller is simple, most of the industrial control problem can be solved; the robust conservatism is, however, rather large to eliminate the resonance peaks with a fixed set of the parameters. To sum up, the whole H-inf controller contains the design of the weighting functions, W_1 and W_2, and the feedback matrix, K. The weighting functions W_1 and W_2 are selected according to the frequency dependence characteristics of the DSA-AVIS as shown in Figure 5. Then the feedback matrix K is obtained by calculating an H-inf norm.

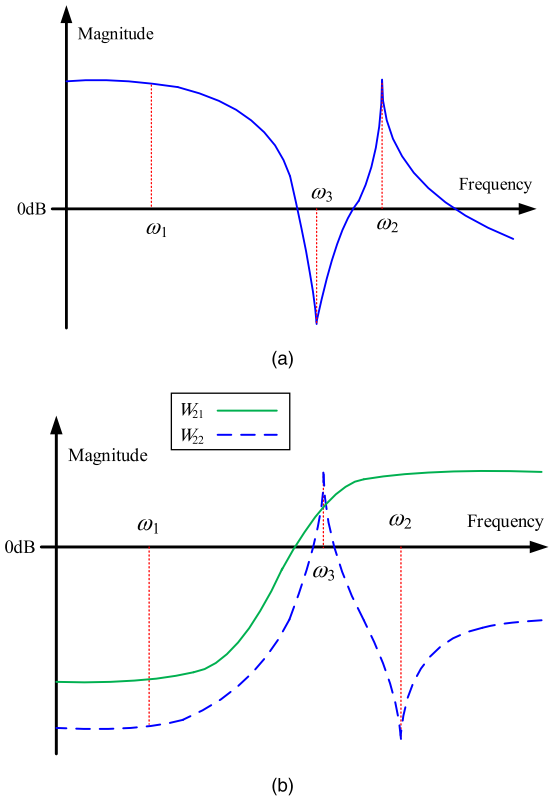

FIGURE 5. Conceptual Bode diagram of the weighting function (a) $\boldsymbol{W_1}$; (b) $\boldsymbol{W_2}$.

IV. EXPERIMENTAL VERIFICATIONS

Figure 6 and **Figure 7** show the designed DSA-AVIS and the PZT, whose parameters are listed in **Table I**. The DSA-AVIS maintains a spring, a payload, a PZT stack, a pair of ari-float rails, a connecting plate, a VCM, and a base. The spring is used to compensate the gravity of the payload. The air-float rails can minimize the friction in the vertical direction. The PZT stack and the VCM are connected in series. A disk spring is also applied to exactly adjust the equivalent stiffness of the PZT stack, which is fixed between the PZT stack and the mover of the VCM. The carefully-designed PZT stack contains an output rob, a front cover, a pre-tightening spring, a linear bearing, a cover, a piezoceramic, and a back cover. The input voltage is applied on the surface of the piezoelectric ceramics, which will then shrink or extend along with the applied voltage. The force generated by the piezoelectric ceramics will be applied on the payload with the aid of the output rob. The pre-tightening spring is used to generate the perforce on the piezoceramic stack.

The equivalent stiffness of the whole PZT is rather lower than the single piezoelectric ceramics due to the existence of the pre-tightening spring. The experimental system is

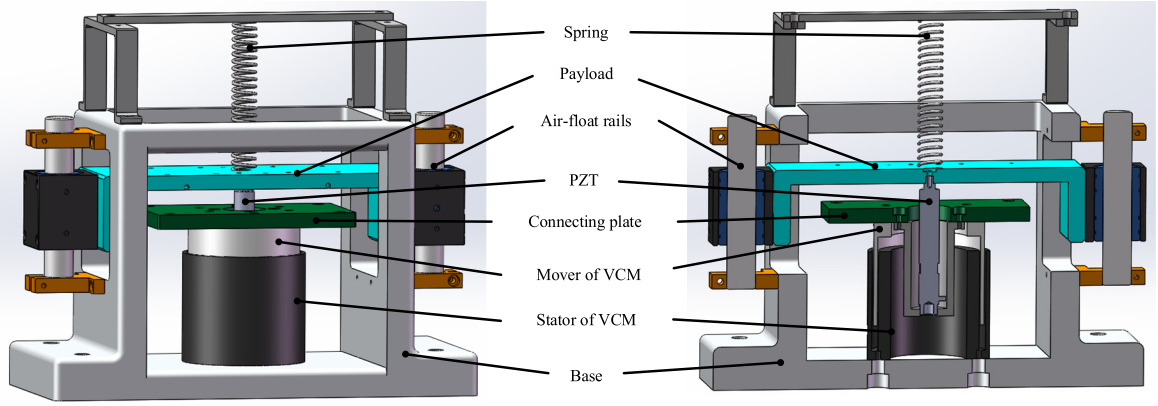

FIGURE 6. The designed DSA-AVIS.

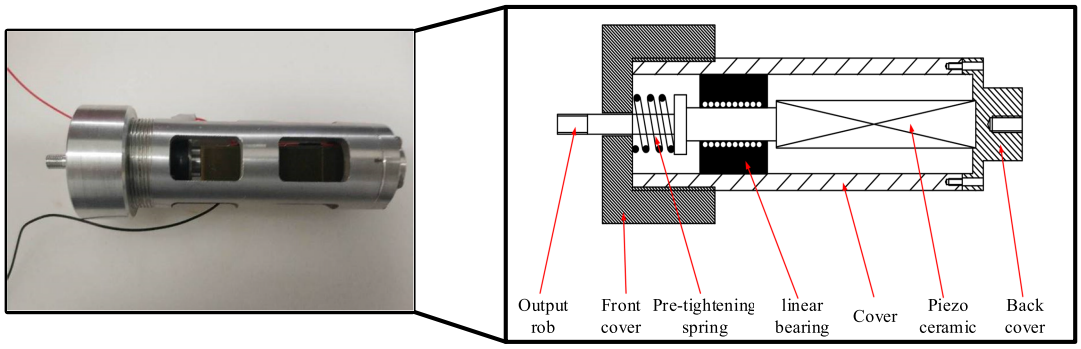

FIGURE 7. Photo and sectional sketch of PZT in DSA-AVIS.

TABLE 1. Parameters of the DSA-AVIS.

Parameter	Value
M	2 kg
m_1	0.9 kg
K	10000 N/m
C	0 N/(m/s)
k_i	31.8 N/A
k_u	9 N/V
k_p	937500 N/m

subsequently built as sketched in **Figure 8**, which is used to verify the characteristic of the DSA-AVIS. The real time target machine is the core component of the whole experimental system, which is designed to respectively send control instruction to the drives of the VCM and the PZT. The TA115 type current amplifier and the E01 type voltage amplifier serve as the drive of the VCM and the PZT, respectively. Moreover, the real time target machine also receives the measurements from GS-11D velocity sensor. The velocity sensor is fixed on the surface of the experimental setup with the aid of a magnet at the bottom of the velocity sensor. The controller is accomplished based on the MATLAB/Simulink software in the computer, which will be downloaded into the real time target machine as well.

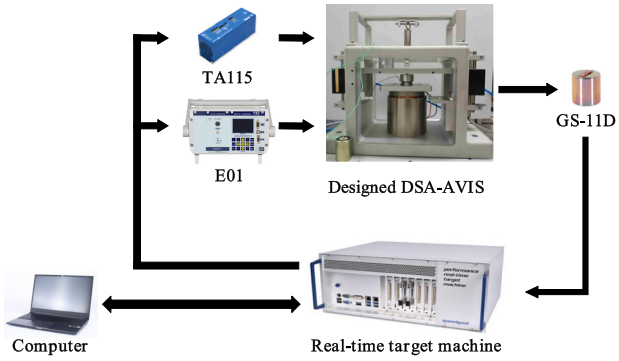

FIGURE 8. Experimental system.

A. CALCULATING CONTROLLER PARAMETERS BASED ON EXPERIMENTAL MEASUREMENTS

The transmissibility from the basement to the payload of the DSA-AVIS is firstly measured as shown in **Figure 9**. The external vibration is generated from hitting the basement by a harmer, which is detected and analyzed by a 941B type vibration analyzer. As shown in Figure 8, two resonance and one antiresonance frequencies are approximately 2.8 Hz, 22.5 Hz, and 11.6 Hz. The transmissibility around the antiresonance frequency is obviously damped. The properties of the weighting functions can be subsequently selected as discussed in

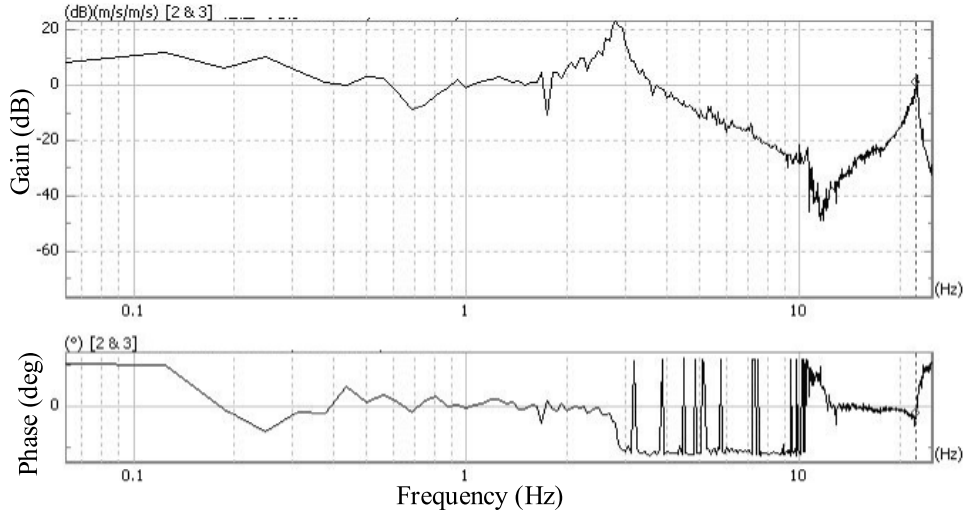

FIGURE 9. Transmissibility curve without controller.

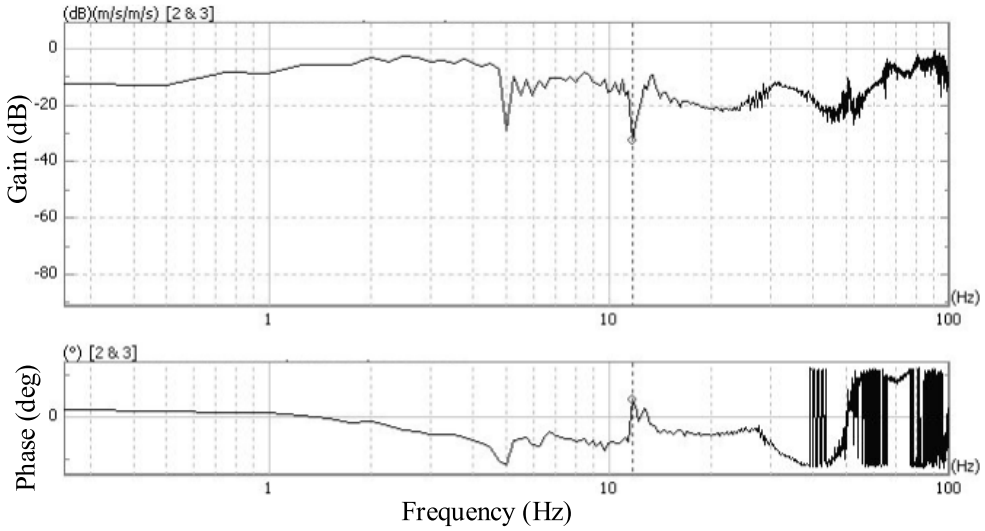

FIGURE 10. Transmissibility curve with controller.

Section III. The current range of the VCM is from −1.67 to 1.67 A, and the voltage range of the PZT is from 0 to 100 V. The work frequency band of the VCM is from 0 to 5 Hz, approximately, and work frequency band of the PZT is from 0 to 40 Hz, approximately.

Hence, the weighting functions can be eventually identified as,

$$\boldsymbol{W_1} = \frac{3140.7\left(s^2 + 0.1s + 1.042 \times 10^6\right)}{(s + 62.83)\left(s^2 + 5s + 1.512 \times 10^6\right)}$$

$$\boldsymbol{W_2} = \begin{bmatrix} W_{21} & 0 \\ 0 & W_{22} \end{bmatrix}$$

$$W_{21} = \frac{5\left(s^2 + 178.4s + 1.579 \times 10^4\right)}{s^2 + 1.784 \times 10^4 s + 1.579 \times 10^8}$$

$$W_{22} = \frac{0.05\,(s + 62.84)\left(s^2 + 10s + 1.512 \times 10^6\right)}{\left(s + 3.14 \times 10^4\right)\left(s^2 + 0.1s + 1.042 \times 10^6\right)}$$

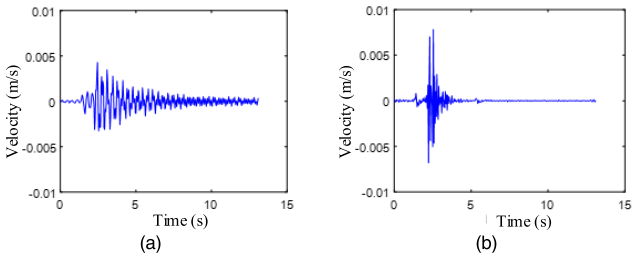

FIGURE 11. Velocities of payload and basement without controller. (a) Payload. (b) Basement.

B. EXPERIMENTAL VERIFICATION OF VIBRATION ISOLATING

Figure 10 indicates that the resonance peaks are eliminated by introducing the well-designed control loop. The transmissibility from the basement to the payload of the DSA-AVIS is consistently lower than 0 dB.

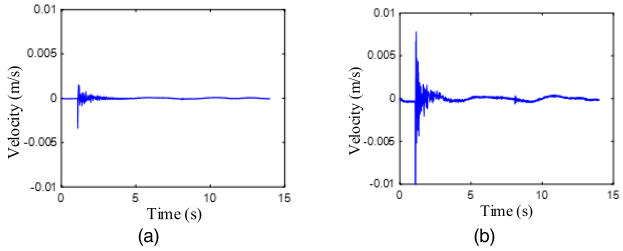

FIGURE 12. Velocities of payload and basement with controller. (a) Payload. (b) Basement.

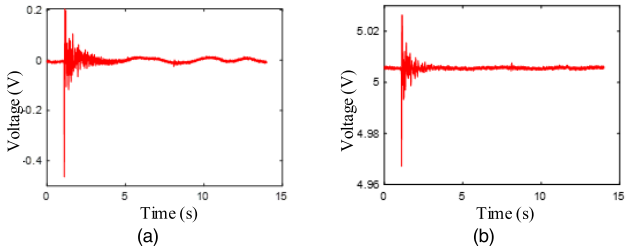

FIGURE 13. Control voltages of VCM and PZT. (a) VCM. (b) PZT.

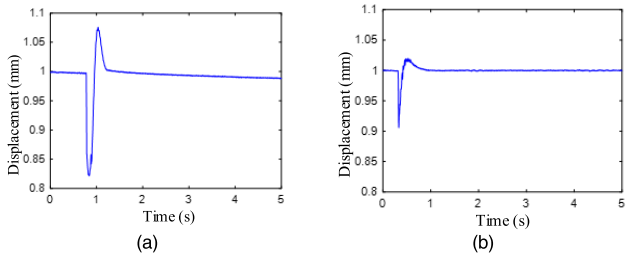

FIGURE 14. Maximum displacement of payload. (a) Without controller. (b) With controller.

Comparing **Figure 11** and **Figure 12** infers that the designed controller is effective to eliminate the external disturbance with almost identical amplitudes. As the controller is applied, the vibration amplitude of the payload reduces to 1.3 mm/s, which is only 32.5% of that without controller. The control voltages of the VCM and the PZT of the DSA-AVIS are sketched by **Figure 13**. The control voltages refer the input voltage of the drive of the VCM and the PZT; that is, the curves in the Figure 13 are the input voltage of the TA115 type current amplifier and the E01 type voltage amplifier, respectively. The input current and the input voltage of the VCM and the PZT are subsequently generated by the TA115 type current amplifier and the E01 type voltage amplifier. The displacement of the payload is sketched in **Figure 14**, which indicates that the maximum displacement is reduced to 0.093 mm from 0.178 mm by 47.75%.

To sum up, the proposed DSA-AVIS with the well-designed H_∞ controller maintains ability to actively isolate the external vibration disturbance within a considerable bandwidth.

V. CONCLUSION

In this paper, a novel dual-stage actuator is proposed. The dual-stage actuator maintains the advantages in terms of long stroke, high precision and wide band by combining the VCM and the PZT. A DSA-AVIS with the proposed dual-stage actuator is initially modeled. The anti-resonance characteristic of the DSA-AVIS can be utilized to save energy. A $H\infty$ controller is designed to consider the vibration isolation performance and the output range of the actuators. The simulation results show that the closed-loop transmissibility is less than -18 dB from 0 to 100 Hertz. This means the proposed DSA-AVIS with the designed $H\infty$ controller has good vibration isolation performance.

REFERENCES

[1] H. Bulter, "Position control in lithographic equipment an enabler for current-day chip manufacturing," *IEEE Control Syst. Mag.*, vol. 31, no. 5, pp. 28–47, Oct. 2011.
[2] S. Ito, S. Unger, and G. Schitter, "Vibration isolator carrying atomic force microscope's head," *Mechatronics*, vol. 44, pp. 32–41, Jun. 2017.
[3] J. H. Lee, H. Y. Kim, K. H. Kim, M. H. Kim, and S. W. Lee, "Control of a hybrid active-passive vibration isolation system," *J. Mech. Sci. Technol.*, vol. 31, no. 12, pp. 5711–5719, Dec. 2017.
[4] W. Sun, Z. Zhao, and H. Gao, "Saturated adaptive robust control for active suspension systems," *IEEE Trans. Ind. Electron.*, vol. 60, no. 9, pp. 3889–3896, Sep. 2013.
[5] X. Wang, F. Bi, and H. Du, "Reduction of low frequency vibration of truck driver and seating system through system parameter identification, sensitivity analysis and active control," *Mech. Syst. Signal Process.*, vol. 105, pp. 16–35, May 2018.
[6] Y. Xu, H. Liao, L. Liu, and Y. Wang, "Modeling and robust H-infinite control of a novel non-contact ultra-quiet stewart spacecraft," *Acta Astronautica*, vol. 107, pp. 274–289, Feb./Mar. 2015.
[7] W. Chi, D. Cao, D. Wang, J. Tang, Y. Nie, and W. Huang, "Design and experimental study of a VCM-based Stewart parallel mechanism used for active vibration isolation," *Energies*, vol. 8, no. 8, pp. 8001–8019, Aug. 2015.
[8] H. Anajafi and R. A. Medina, "Comparison of the seismic performance of a partial mass isolation technique with conventional TMD and base-isolation systems under broad-band and narrow-band excitations," *Eng. Struct.*, vol. 158, pp. 110–123, Mar. 2018.
[9] C. Song, Y. Xiao, C. Yu, W. Xu, and J. Zhang, "H∞ active control of frequency-varying disturbances in a main engine on the floating raft vibration isolation system," *J. Low Freq. Noise, Vib. Act. Control*, vol. 37, no. 2, pp. 199–215, Jun. 2018.
[10] B. Yang, Y. Hu, and J. Zhang, "Modeling and H_∞ control of active-passive vibration isolation for floating raft system," *Math. Problems Eng.*, vol. 2017, Feb. 2017, Art. no. 5361702.
[11] L. Zuo and J.-J. E. Slotine, "Robust vibration isolation via frequency-shaped sliding control and modal decomposition," *J. Sound Vib.*, vol. 285, nos. 4–5, pp. 1123–1149, Aug. 2005.
[12] J. Tang, D. Cao, F. Ren, and H. Li, "Design and experimental study of a VCM-based whole-spacecraft vibration isolation system," *J. Aerosp. Eng.*, vol. 31, no. 5, Sep. 2018, Art. no. 04018045.
[13] D.-P. Hong, H.-Y. Hwang, M.-Y. Lee, Y.-K. Jo, D.-T. Vu, and D.-Y. Lee, "New electro-magnetic actuator for active vibration isolators," *Int. J. Precis. Eng. Manuf.*, vol. 16, no. 1, pp. 209–212, Jan. 2015.
[14] M. H. Kim, H. Y. Kim, H. C. Kim, D. Ahn, and D.-G. Gweon, "Design and control of a 6-DOF active vibration isolation system using a Halbach magnet array," *IEEE/ASME Trans. Mechatronics*, vol. 21, no. 4, pp. 2185–2196, Aug. 2016.
[15] S. Ito and G. Schitter, "Atomic force microscopy capable of vibration isolation with low-stiffness Z-axis actuation," *Ultramicroscopy*, vol. 186, pp. 9–17, Mar. 2018.
[16] S. Ito and G. Schitter, "Comparison and classification of high-precision actuators based on stiffness influencing vibration isolation," *IEEE/ASME Trans. Mechatronics*, vol. 21, no. 2, pp. 1169–1178, Apr. 2016.
[17] L. Zhang, Z. Long, J. Cai, and J. Fang, "Design of a linear macro–micro actuation stage considering vibration isolation," *Adv. Mech. Eng.*, vol. 7, no. 5, pp. 1–13, May 2015, Art. no. 1687814015584541.
[18] Y. Kong and H. Huang, "Vibration isolation and dual-stage actuation pointing system for space precision payloads," *Acta Astronautica*, vol. 143, pp. 183–192, Feb. 2018.

[19] Y. Zhang, Z. Chen, and Y. Jiao, "A hybrid vibration isolator: Design, control, and experiments," *Proc. Inst. Mech. Eng., C, J. Mech. Eng. Sci.*, vol. 230, no. 17, pp. 2982–2995, Oct. 2016.
[20] C. Wang, X. Xie, Y. Chen, and Z. Zhang, "Investigation on active vibration isolation of a Stewart platform with piezoelectric actuators," *J. Sound Vib.*, vol. 383, pp. 1–19, Nov. 2016.
[21] J. Fu, P. Li, G. Liao, J. Lai, and M. Yu, "Active/semi-active hybrid isolation system with fuzzy switching controller," *J. Intell. Mater. Syst. Struct.*, vol. 29, no. 1, pp. 101–115, Jan. 2018.
[22] Y.-T. Liu, R.-F. Fung, and C.-C. Wang, "Precision position control using combined piezo-VCM actuators," *Precis. Eng.*, vol. 29, no. 4, pp. 411–422, Oct. 2005.
[23] Y. Liu, T. Li, and L. Sun, "Design of a control system for a macro-micro dual-drive high acceleration high precision positioning stage for IC packaging," *Sci. China E, Technol. Sci.*, vol. 52, no. 7, pp. 1858–1865, Jul. 2009.
[24] L. Zhang, J. Gao, and X. Chen, "A rapid dynamic positioning method for settling time reduction through a macro–micro composite stage with high positioning accuracy," *IEEE Trans. Ind. Electron.*, vol. 65, no. 6, pp. 4849–4860, Jun. 2018.
[25] C. Liu, D. Xu, J. Zhou, and S. Bishop, "On theoretical and experimental study of a two-degree-of-freedom anti-resonance floating vibration isolation system," *J. Vib. Control*, vol. 21, no. 10, pp. 1886–1901, Jul. 2015.

BO ZHAO received the B.Sc., M.Sc., and Ph.D. degrees in mechatronics engineering from the Harbin Institute of Technology (HIT), Harbin, China, in 2004, 2006, and 2011, respectively, where he has been with the Center of Ultra-Precision Optoelectronic Instrument Engineering, since 2012.

His research interests include vibration isolation systems, piezoelectric drive technology, and adaptive robust control.

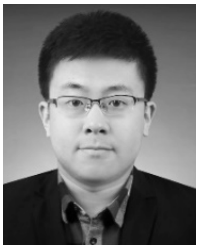

WEIJIA SHI received the B.Sc. degree in control science and engineering from Northwestern Polytechnical University, Xi'an, China, in 2009, and the M.Sc. and Ph.D. degrees in control science and engineering from the Harbin Institute of Technology (HIT), Harbin, China, in 2011 and 2017, respectively.

From 2014 to 2015, he was a joint Ph.D. Student with Pennsylvania State University at State College, PA, USA. Since 2017, he has been with the Center of Ultra-Precision Optoelectronic Instrument Engineering, HIT. His research interests include modeling of losses within piezoelectrics and related actuators, and designs of unique drivers and controllers for piezoelectric actuators.

JIUBIN TAN received the B.Sc., M.Sc., and Ph.D. degrees in instrument science and technology from the Harbin Institute of Technology (HIT), Harbin, China, in 1982, 1987, and 1991, respectively, where he has been with the Department of Instrument Science and Engineering, since 1991.

He was an Elected Member of the CAE Inc., in 2017. He has 132 granted patents including 21 international patents. He has drafted 26 standards, published more than 310 EI and SCI articles, and authored 3 monographs. His research interests include precision measurement and instrument technology, ultra-precision opto-mechatronics equipment technology, and precision laser measurement technology.